

See discussions, stats, and author profiles for this publication at: <https://www.researchgate.net/publication/23141646>

Europium(3+): An Efficient Luminescence Probe for the Si to Al Ratio and Silylation Effects in the Microporous–Mesoporous Zeogrid Materials

ARTICLE in THE JOURNAL OF PHYSICAL CHEMISTRY B · SEPTEMBER 2008

Impact Factor: 3.3 · DOI: 10.1021/jp711337h · Source: PubMed

CITATIONS

8

READS

38

6 AUTHORS, INCLUDING:



Carmen Tiseanu

National Institute for Laser, Plasma and Ra...

66 PUBLICATIONS 613 CITATIONS

SEE PROFILE

Europium(3+): An Efficient Luminescence Probe for the Si to Al Ratio and Silylation Effects in the Microporous–Mesoporous Zeogrid Materials

C. Tiseanu,^{*,†} M. U. Kumke,[‡] V. I. Parvulescu,[§] A. Gessner,[‡] B. Gagea,^{||} and J. Martens^{||}

National Institute for Laser, Plasma and Radiation Physics, P.O. Box MG-36, RO 76900, Bucharest–Magurele, Romania, Institute of Chemistry, Physical Chemistry, University of Potsdam, Karl-Liebknecht-Strasse 24-25, 14476 Potsdam–Golm, Germany, Department of Chemical Technology and Catalysis, University of Bucharest, 4-12 Regina Elisabeta Boulevard, Bucharest 030016, Romania, and Centre for Surface Chemistry and Catalysis, Katholieke Universiteit Leuven, 23 Kasteelpark Arenberg, B-3001 Leuven (Heverlee), Belgium

Received: November 30, 2007; Revised Manuscript Received: March 26, 2008

The optical response of europium ions in the parent (non-silylated) and silylated microporous–mesoporous Zeogrid materials was investigated in detail in relation to Zeogrid structure. All materials were characterized using nitrogen adsorption isotherms, powder X-ray diffraction (PXRD), Fourier transform infrared spectroscopy (FT-IR), thermogravimetry, and time-resolved photoluminescence spectroscopy. A two europium species distribution with distinct luminescence spectra and lifetimes was found for both parent and silylated Zeogrid. In the parent Zeogrid, the short-lived europium species is characterized by the intensity ratio $R = I(^5D_0 - ^7F_2)/I(^5D_0 - ^7F_1)$ or asymmetry values of ~ 0.4 – 0.7 and photoluminescence (PL) lifetimes of 110 – $125\ \mu\text{s}$ and therefore is assigned to an almost fully hydrated europium species. In the silylated Zeogrid, the short-lived europium species is characterized by asymmetry values of 1.0 – 2.4 and lifetimes of 160 – $180\ \mu\text{s}$ suggesting a relatively distorted europium environment. The long-lived europium species exhibits similar asymmetry ratios in the parent and silylated Zeogrid, which vary between 5.0 and 6.2 with increasing Si to Al ratio from 25 to 150 and slightly different PL lifetimes. The mechanism responsible for the intensity of the electric and magnetic forbidden $^5D_0 - ^7F_0$ transition was determined to be J -mixing of the 7F_2 into the 7F_0 state through the axial second-order crystal-field potential. The comparison between the photoluminescence properties of europium in the parent and silylated Zeogrid demonstrates that the effects of rehydration were strongly suppressed following silylation.

I. Introduction

Since their discovery in the early 1990s, ordered mesoporous materials have attracted great interest due to their unique properties, e.g., large uniform pore structures, high specific surface areas, and specific pore volumes.^{1–3} Numerous applications for these materials have been found, including adsorption, sensing, catalysis, separation, medical usage, ecology, clean energy applications, and nanotechnology. In the literature various methodologies for synthesis of the mesoporous materials were reported. These cover a large range from the traditional template approaches that assemble micelles as a template to replica synthesis approaches.^{4–7}

With the introduction of various coordination or supramolecular structures into the mesopores, new photoelectronic functions became available.⁸ An increasing number of reports are devoted to the use of ordered mesoporous silica materials as a support for organic complexes of lanthanides.^{9–29} One of the most studied hosts for lanthanide complexes is MCM-41;^{10–16,18,23–27} on the other hand SBA-15^{9,21,22,28} or MCM-48^{17,19} are less studied. Weak physical interactions between the host and the incorporated lanthanide complex can debase the photoluminescence (PL) properties of the obtained materials,

due to clustering of the emitting centers, inhomogeneous dispersion of the organic and metallic components, or leaching of the photoactive molecules. To overcome such disadvantages, new synthesis approaches are reported. For example, the synthesis of mesoporous silica MCM-41 covalently attached to a binary europium (Eu^{3+}) complex with the phen ligand (1,10-phenanthroline) via a cocondensation process leads to a higher and more homogeneous surface coverage of the organosilane functionalities and could effectively prevent the aggregation of lanthanide complexes.¹⁶ SBA-15 appears to be more attractive as an embedding host for the lanthanide's complexes than MCM-41 because of its much larger uniform pore size (up to $30\ \text{nm}$), thicker silica wall, and better stability. Recently, the synthesis of a luminescent mesoporous SBA-15 silica covalently linked to a europium(TTA)₃phen complex (with $\text{TTA} = 2$ -thenoyltrifluoroacetone) was reported, which shows a strong Eu^{3+} emission and a good thermal stability.²² The substitution of the silanols for the covalently linked phen groups in the pore channels of the mesoporous SBA-15 leads to the decrease of the nonradiative multiphonon relaxation by coupling to $-\text{OH}$ vibrations. By using the ion-exchange method, a first luminescent lanthanide complex, $\text{Eu}^{3+}(\text{phen})_2\text{Cl}_3 \cdot 2\text{H}_2\text{O}$, incorporated in the channels of a silylated mesoporous MCM-41 silica was obtained.¹⁵ The passivation of the silanols ensures that the ion-exchange reaction occurs only between the lanthanide complex ions and the surfactant cations *inside* the channels of the modified MCM-41. Silylation was also used in the preparation of a luminescent mesoporous MCM-48 silica impregnated with

* Corresponding author.

[†] National Institute for Laser, Plasma and Radiation Physics.

[‡] University of Potsdam.

[§] University of Bucharest.

^{||} Katholieke Universiteit Leuven.

europium–dibenzoylmethane complexes.¹⁹ The energy of the charge-transfer (CT) band of europium in mesoporous host material could be changed due to silylation, and subsequently the efficiency of the thermal quenching via the CT state can be reduced. Generally, the organic ligands were sought to protect the lanthanide ions from water molecules present under ambient conditions in mesoporous materials obtained via sol–gel processes and to sensitize the lanthanide luminescence (via the antenna effect). On the other side, besides changing the porous and adsorption properties, silylation of the mesoporous materials could reduce the luminescence quenching by the hydroxyl groups on the surface and improve the hydrothermal stability.^{30–36}

For the lanthanide ions exchanged in zeolites or mesoporous materials without a coordinating organic ligand, the luminescence properties can be improved by calcinations. However, upon exposure to moist atmosphere, the PL properties characteristic for the hydrated state will be partially restored.^{37–40} Current work on terbium-exchanged zeolites showed that following the silylation of the calcined terbium-exchanged BEA, USY, MOR, and ZSM-5 zeolites^{41–43} with hexadecyl-, phenyl-, and vinyltrimethoxysilanes, luminescence properties were preserved more or less at the values measured after the calcination. The characterization of these materials indicated a significant reduction of the chemisorbed water due to silylation.

Here, the calcined europium-exchanged Zeogrid materials with Si to Al ratio = 25, 50, 100, and 150 were silylated with hexadecyltrimethoxysilanes via postsynthesis grafting. In comparison to MCM-41, MCM-48, or SBA-15, the microporous–mesoporous Zeogrid material contains two levels of porosity, one provided by the structure of the MFI building blocks and the second one generated by the association of the MFI building blocks forming the Zeogrid structure.^{44–47} Besides high luminescence efficiency, the distribution of the europium ions and the nature of the local microenvironment at the dopants sites represent the key parameters to be considered in relation with the optical applications of these materials. The europium ion has been chosen because the intensity of its emission bands strongly depends on the strength and symmetry of the crystal field around the europium ion, being widely used as a tool in describing the structure and properties of disordered media.^{48–66}

The aim of present paper is twofold (i) to assess the silylation efficiency and (ii) to use the lanthanide ion as a luminescence probe for the host–dopant interactions. The europium species were characterized in detail in both parent and silylated Zeogrid in terms of characteristic PL lifetimes, local crystal-field environment, and the constitution of the first coordination shell. The mechanism responsible for the intensity of the electric and magnetic forbidden ⁵D₀–⁷F₀ transition was determined. Finally, from the comparison between the average PL lifetimes and the relative intensities of emission transitions related to ⁵D₀ and ⁵D₁ levels in the silylated and non-silylated Zeogrid the effects of the silylation were inferred. All materials were investigated by infrared Fourier transform (FT-IR), powder X-ray diffraction (PXRD), adsorption–desorption isotherms of N₂ at 77 K, thermogravimetry (TG), and time-resolved luminescence spectroscopy (TRES).

II. Experimental Section

II.1. Materials Synthesis. Details on synthesis of ZG materials were given elsewhere.^{44,45} Ion exchange was performed by adding 1 g of structured material in 25 mL of 0.004 M europium aqueous (nitrate) solution and stirring for 30 min at 80 °C. The samples were then recuperated, washed until free of europium, and dried in air at 50 °C for 2 days. Calcination

was pursued in air at 450 °C at a heating rate of 5 °C/min. The europium–ZG samples were denoted as *parent* or *non-silylated* materials. Silylation of the above samples was carried out by stirring 1 g of calcined europium-exchanged Zeogrid material in 10 mL of toluene (previously dried with 5 Å molecular sieves). Next, 2 mL of hexadecyltrimethoxysilane or C₁₆ (used as received) was added to this suspension under continuous stirring at room temperature for 24 h. The grafted materials were then filtered, washed with toluene, and then dried at 100 °C under vacuum. The obtained europium–ZG samples were denoted as *silylated*.

II.2. Materials Characterization. Structural characterization of the investigated samples was performed using nitrogen adsorption isotherms at –196 °C, thermogravimetry, FT-IR, and PXRD. The specific surface areas of the samples and the volume were determined from the nitrogen adsorption isotherms using the micropore program with a Micromeritics ASAP2020 instrument, after degassing the samples in situ at 120 °C for 5 h. PXRD patterns were collected on a Siemens D-5000, using Cu K α radiation ($\lambda = 1.54050$ Å) and quartz as an external standard. DRIFT spectra were collected with a Nicolet 4700 FT-IR instrument using the KBr pellet technique during heating the samples in helium with a rate of 1 °C/min with a plateau of 1 h at each measuring temperature. Thermogravimetric analysis curves (thermogravimetric (TG) and heat flow) were measured by using a SETARAM 92 16.18 apparatus in air using a heating rate of 10 °C/min.

II.3. Photoluminescence Measurements and Analysis. Time-resolved emission spectra (TRES) were recorded using a wavelength-tunable Nd:YAG laser/OPO system (Spectra Physics/GWU) operating at 20 Hz as excitation light source and an intensified CCD camera (Andor Technology) coupled to a spectrograph (MS257 model 77700A, Oriel Instruments) as detector. The TRES were collected using the box car technique. In a typical experiment the sample was non-selectively excited at 394 nm (corresponding to the ⁷F₀–⁵L₆ transition), the initial gate delay (delay after the laser pulse) was set to 2 μ s, and the gate width was adjusted to 50 μ s. The gate delay was increased non-linearly with time to obtain closely spaced emission spectra at short times and more spaced in time emission spectra at longer times after excitation. This accounted for data oversampling with positive effect on the reduction of the uncertainty of the decay deconvolution. The PL was detected in the spectral range of 500 nm < λ_{em} < 750 nm with a maximum spectral resolution of 0.08 nm. All PL measurements were performed at room temperature. The PL decays were analyzed by (1) fitting of the integrated PL decays within wavelength intervals corresponding to the different europium luminescence transitions with a multiexponential function, $f(t)$:

$$f(t) = \sum_{i=1}^n A_i \exp(-t/\tau_i) + B \quad (1)$$

where A_i is the decay-related amplitude, B is a constant (the baseline offset), and τ_i is the lifetime. The average PL lifetimes were calculated using the following formula:

$$\langle \tau \rangle = \frac{\sum_{i=1}^n A_i \tau_i}{\sum_{i=1}^n A_i} \quad (2)$$

and (2) using the quantified maximum entropy method, MaxEnt, of the commercial software package Pulse 5 (Maximum Entropy Data Consultants, Ltd., version 1998). The program inverts fluorescence decay data to produce a spectrum of lifetimes. The integrated area of the TRES within various wavelength intervals

TABLE 1: Chemical Composition and Textural Properties of the Parent and Silylated Europium–ZG

Si/Al ratio	Eu ³⁺ content (wt %)	BET surface of Eu ³⁺ –ZG precursor (m ² g ^{−1}) ^a	C ₁₆ content (wt %) ^a	BET surface (m ² g ^{−1}) ^a
25	0.73	1580	23.1	910
50	0.64	1630	23.4	930
100	0.41	1650	23.0	940
150	0.34	1660	23.2	960

^a Determined from TG measurements.

was analyzed by providing the distribution of exponential amplitudes versus exponential time constants. A detailed introduction to the quantified maximum entropy method for time-resolved fluorescence data analysis is given in ref 67. The number of bands recovered in the MaxEnt lifetime distribution represents the number of resolvable decay components in the data, whereas the band positions and band areas of the MaxEnt lifetime distribution give the corresponding lifetimes and amplitudes of the components.

Through the text, the lifetimes and amplitude are presented as the average of triplicate measurements from the same sample. Generally, standard deviation was less than 5% for the lifetimes and 7% for the amplitudes.

III. Results and Discussion

III.1. Structural Characterization. Table 1 presents the chemical composition and textural properties of the parent and silylated europium–ZG materials. Typical adsorption–desorption isotherms for these materials are given in the Figure 1a. Deposition of the Eu³⁺ was not accompanied by any specific textural changes. Since the metal loading was very small, the changes in the surface area for the materials can be attributed directly to the different Si/Al ratios. Silylation was accompanied by a significant decrease of the surface area corresponding to a partial blockage of the pores by the trimethoxysilane agent. Again, the controlling factor for the changes in the BET surface area was the Si/Al ratio, as the extent of silylation was similar for all samples. The micropore volume of the Zeogrid samples was calculated from the *t*-plot analysis based on the adsorption isotherms and was found to be in the range of 0.6–0.7 mL/g. Zeogrid samples exhibit two types of micropores. Analysis of the adsorption isotherm at $p/p_0 < 3.5 \times 10^{-4}$ confirms that the Zeogrid materials contain the same type of micropores as the MFI zeolites. In addition to these micropores, Zeogrid samples also contain a type of supermicropore resulting from the stapling of the zeolite precursor units. The size of micropores was calculated to be around 1.5 nm which is in good agreement with the determined size for the zeolite precursors^{44,47}

Figure 1b shows the PXRD patterns of two samples before and after silylation. Samples presented a typical PXRD pattern for a Zeogrid-type material.⁴⁴ The pattern can be associated to a lamellar structure with a distance of 3.2 nm between the MFI planes (corresponding to the maximum reflection from $2\theta = 2.7$). For the silylated sample, the signal broadening and the shift of the maximum toward higher *d* values (corresponding to lower 2θ angles) is assigned to a certain swelling of the layered structure due to the presence of the hydrocarbon chain. A similar behavior has been found for all the materials investigated. FT-IR spectra confirmed the successful deposition of the silylating agent. The FT-IR spectra of a Zeogrid and the corresponding silylated sample in the region of 4000–2000 cm^{−1} are presented in Figure 1c. Zeogrid sample presents only a broad adsorption band in the region of 3000–3500 cm^{−1} which

is assigned to various types of O–H bonds. These O–H bands can be attributed to either various silanol groups (terminal, geminal, bridged,...) or to the physically adsorbed water on the surface of the material. The silylated sample showed a much lower intensity band in the silanol region, which can be assigned to the water desorption during the calcination step. Immediately following the calcination step, the samples were functionalized with the hexadecyl groups in order to block the access of water in the pores and hydrate the europium ions; thus, absorption of water on these samples was suppressed. In addition to the silanol absorption band, the silylated sample presents two bands at 2930 and 2860 cm^{−1} which are attributed to the C–H bonds present in the C₁₆ hydrocarbon chain. These bands also confirm the successful incorporation of the organic groups on the Zeogrid materials.

As expected, the silylation of these materials strongly suppress the interaction with water. Figure 1d shows the TG (denoted with a) and heat flow curves (denoted with b) for the parent (upper) and silylated europium–ZG(25) (bottom) samples. Both the mass loss and corresponding heat flow were reduced following silylation. For example, mass loss at 100 or 200 °C is about 0.4 and 0.7 mg, respectively (Figure 1d, bottom). These values should be compared with those obtained with the parent europium–ZG (1 or 2.1 mg), Figure 1d, upper.

III.2. Photoluminescence Properties. III.2.1. Parent (Non-silylated) Europium–ZG. Figure 2 shows the PL spectra of the parent europium–ZG following the non-selective excitation at $\lambda_{\text{ex}} = 394$ nm at a delay of $\delta t = 2 \mu\text{s}$ after the excitation. The emission contains the ⁵D₀–⁷F_{*J*} (*J* = 0, 1, 2, 3, 4) transitions at about $\lambda_{\text{em}} = 579, 582, 614, 653,$ and 698 nm as well as ⁵D₁–⁷F_{*J*} transitions (*J* = 0, 1, 2) at about $\lambda_{\text{em}} = 524, 535,$ and 555 nm. The detection of the emission related to the ⁵D₁ state indicates that the non-radiative relaxation from the ⁵D₁ to the ⁵D₀ state is not very efficient in these materials. In high-resolution spectra all transitions show an internal structure with more or less resolved components.

The samples were also selectively excited in the wavelength range $565 \text{ nm} < \lambda_{\text{ex}} < 585 \text{ nm}$. Figure 3 illustrates the spectral shift corresponding to the peak emission of the ⁵D₀–⁷F₂ transition under selective excitation within this interval. The peak emission was shifted from $\lambda_{\text{em}} = 617.5$ nm ($\lambda_{\text{ex}} = 579$ nm) to $\lambda_{\text{em}} = 622.5$ nm ($\lambda_{\text{ex}} = 571$ nm) or 618 nm ($\lambda_{\text{ex}} = 565$ nm). The observation of europium PL following excitation at lower energy than that corresponding to the ⁷F₀–⁵D₀ transition (i.e., $580 \text{ nm} < \lambda_{\text{ex}} < 585 \text{ nm}$) confirmed that the ⁷F₁ level is thermally populated. For europium-doped glasses a variation of the ⁵D₀–⁷F₂ emission peak position with excitation energy has been observed. It was attributed to different local europium environments that emit following selective excitation.^{66,68,69,77}

The TRES show a dependency on the Si/Al ratio, excitation wavelength λ_{ex} , delay time δt after the laser pulse, and silylation treatment, respectively. All these changes are discussed below.

III.2.1.1. ⁵D₀–⁷F₀. The electric and the magnetic forbidden ⁵D₀–⁷F₀ transition is detected as a weak shoulder on the ⁵D₀–⁷F₁ transition in all the parent europium–ZG (Figure 2). As there is no crystal-field splitting of the ⁵D₀ and ⁷F₀ levels, this transition is an effective probe of the bonding environment of the europium ions providing information on the number of the emissive species.

The ⁵D₀–⁷F₀ transition shows, besides the dependence of its spectral line shape on the Si/Al ratio, the following features (Figure 4, parts a and b): (i) a structure with two peaks located at about $\lambda_{\text{em}} = 578$ and 579 nm, (ii) a pronounced asymmetry at the lower-wavelengths side, (iii) a relative large peak width

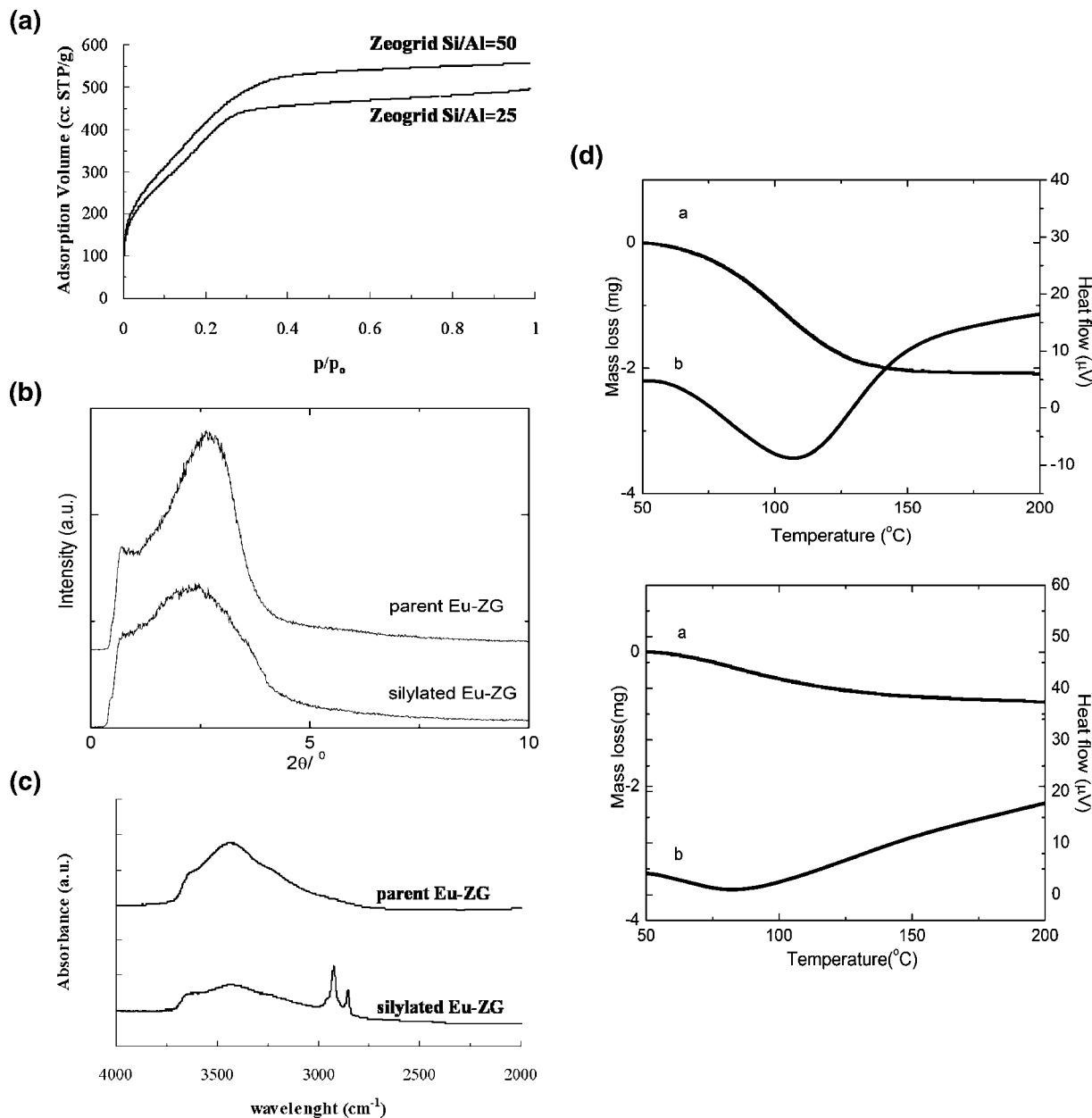


Figure 1. (a) Nitrogen adsorption isotherms for the europium-ZG. (b) PXRD patterns of the parent and silylated europium-ZG. (c) FT-IR spectra of the parent and silylated europium-ZG. (d) The mass loss (curves a) and heat flow (curves b) for (upper) the parent ($m = 20.27$ mg) and (bottom) silylated Eu³⁺-ZG(25) ($m = 35.38$ mg).

(FWHM about 3.3–3.5 nm), and (iv) the spectral line shape depends on the delay time after the laser pulse (δt). FWHM value of the 5D_0 – 7F_0 transition (about 100 cm⁻¹) in the parent europium-ZG is close to that usually measured in glasses. Further, the asymmetry of this transition is attributed to the inhomogeneous broadening of this line induced by the distribution of the crystal-field strength at the dopant sites (e.g., the distribution of the values of the second-rank crystal-field parameters B_{20}).^{70–72} Albeit the effects of the Si/Al ratio on the intensity and spectral shape of this transition could not be properly quantified due to the low intensity of this transition a trend in the increase of the relative intensity of the shoulder at $\lambda_{em} = 578$ nm to that at $\lambda_{em} = 579$ nm with increasing Si/Al ratio was observed (Figure 4a). A more explicit trend was found in the spectral-shape evolution of the 5D_0 – 7F_0 transition with delay time δt (Figure 4b). At $\delta t = 1$ ms the emission is shifted toward shorter wavelengths compared to $\delta t = 2$ μ s and shows only one emission band with a maximum at about $\lambda_{em} = 577.5$

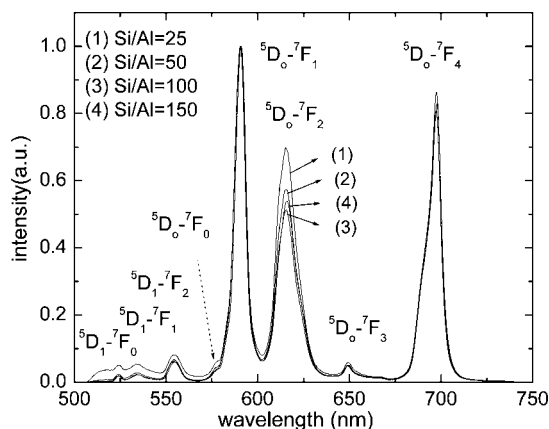


Figure 2. Effects of the Si to Al ratio on the PL spectra of the parent Eu³⁺-ZG. All spectra were normalized to the area corresponding to the 5D_0 – 7F_1 transition.

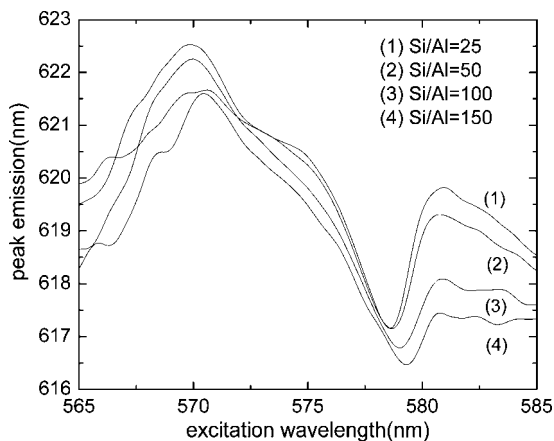


Figure 3. Dependence of the peak emission λ_{em} corresponding to the $^5D-^7F_2$ transition on the excitation wavelength in the spectral range of the $^7F_{0,1}-^5D_0$ absorption bands of the parent $Eu^{3+}-ZG$.

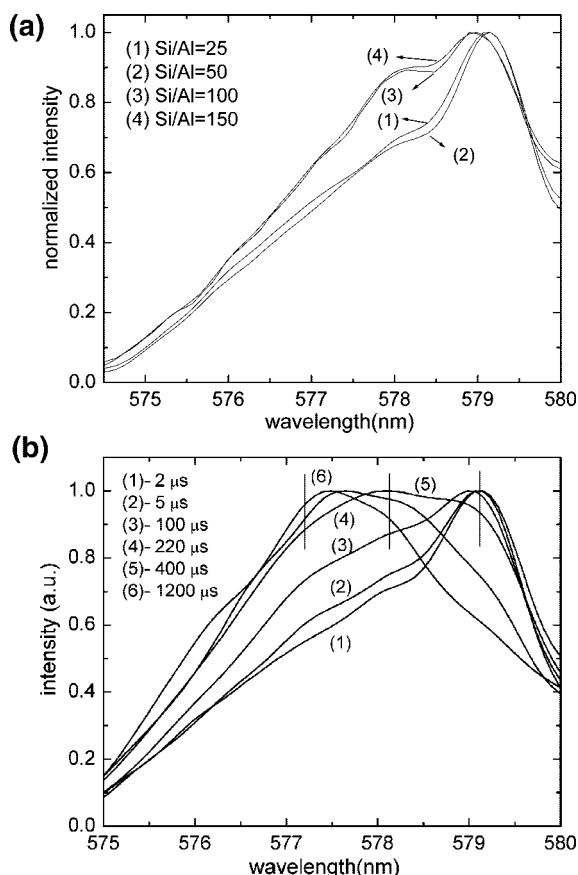


Figure 4. (a) Effects of the Si to Al ratio on the $^5D_0-^7F_0$ emission of the parent $Eu^{3+}-ZG$. (b) Time-resolved PL spectra of the parent $Eu-ZG(25)$ related to the $^5D_0-^7F_0$ transition. The delay times after the laser pulse are indicated in the figure.

nm. The Gaussian deconvolution of the prompt luminescence spectra ($\delta t = 2 \mu s$) gives two different emission components centered at $\lambda_{em} = 577.5$ and 578.7 nm, respectively. The emission centered at $\lambda_{em} = 577.5$ nm is much broader and more intense compared to that centered at $\lambda_{em} = 578.7$ nm FWHM at 3.3 nm compared to 0.5 nm and the relative intensity of $\sim 5-8$ compared to 1. From these results it is concluded that two major europium species with different PL properties contribute to the total luminescence in the parent europium-ZG materials. The present results are in line with our recent findings for terbium in Zeogrid which pointed to a two major species as well, one

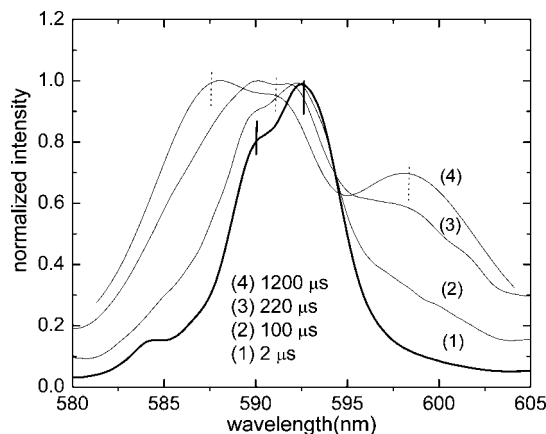


Figure 5. Time-resolved luminescence spectra of the parent $Eu^{3+}-ZG(25)$ related to the $^5D-^7F_1$ transition. The delay times after the laser pulse are indicated in the figure.

located on the internal surface and one inside the pores.³⁸ Further arguments that sustain this assumption are presented in the following sections.

III.2.1.2. $^5D_0-^7F_1$. The $^5D_0-^7F_1$ transition is a magnetic dipole allowed transition, and its intensity scarcely varies with the bonding environment of the europium ions. The width and shape of this transition was analyzed in order to obtain information on the number of Stark levels and to correlate it to the number of luminescent species. As illustrated in Figure 5, the $^5D_0-^7F_1$ emission line shows a fine structure with at least two shoulders at about $\lambda_{em} = 590$ and 592.5 nm (denoted with solid lines in Figure 5). The spectral feature at $\lambda_{em} = 584$ nm is completely quenched after $\delta t = 20 \mu s$, pointing to the interference of luminescence originating from upper levels ($^5D_{1,2}$). With increasing δt , the line shape dramatically changes showing three additional peaks at about $\lambda_{em} = 586$, 592 , and 599 nm (values taken from the PL spectra measured at $\delta t = 1$ ms, marked by dotted lines in Figure 5). In summary, at least 5 peaks are recovered from analysis of the TRES in all parent europium-ZG samples. As the maximum number of splitting levels connected to this transition is three, two europium species with different luminescence decays may be responsible for the observed splitting.

It is generally accepted that the local symmetry of the europium sites in glasses is orthorhombic, which represents the highest symmetry for which the full splitting of the 7F_1 and 7F_2 states of europium is allowed and the lowest in which symmetry of most of the components is maintained.⁷³ We assume the same symmetry for the crystal-field potential H_{CF} acting at the europium sites in Zeogrid materials. The crystal-field potential expressed in the Wybourne notation is

$$H_{CF} = B_{20}C_0^{(2)} + B_{22}(C_{-2}^{(2)} + C_2^{(2)}) \quad (3)$$

where B_{20} and B_{22} are the crystal-field parameters and $C_0^{(2)}$, $C_{-2}^{(2)}$, and $C_2^{(2)}$ are the one-electron spherical tensor operators. If the J -mixing effects are neglected, the diagonalization of the Hamiltonian using the eigenstates of the 7F_1 multiplet gives the following Stark energies:⁷⁴

$$E(\epsilon_0) = E(^7F_1) + B_{20}/5$$

$$E(\epsilon_{\pm}) = E(^7F_1) - (B_{20} \pm \sqrt{6}B_{22})/10 \quad (4)$$

By using eq 2, the following formula for the B_{20} is obtained:

$$B_{20} = \frac{5}{3}[2(E(\epsilon_0) - E(\epsilon_+) - E(\epsilon_-))] \quad (5)$$

where $E(^7F_1)$ denotes the barycenter of the 7F_1 multiplet and $E(\epsilon_0)$, $E(\epsilon_-)$, $E(\epsilon_+)$ denote the energies of the Stark levels of the 7F_1 state. By using a Gaussian deconvolution of the 5D_0 – 7F_1 emission three peak wavelengths at $\lambda_{em} = 585.5$, 592.8 , and 599.6 nm (values corresponding to europium–ZG(150), PL spectra measured at $\delta t = 1$ ms after the laser pulse) were found. All values vary more or less with the delay time δt , whereas the Stark component at about $\lambda_{em} = 585.5$ was found to be the most sensitive (see Figure 5). It is generally assumed that the highest energy feature, which is most sensitive to the excitation energy and usually sharper than the two others, is a transition from the 5D_0 to the $^7F_1(\epsilon_0)$ component of the 7F_1 state.^{70,75} We also adopt this convention. By using eq 5 the calculated B_{20} can be estimated as about 1020 cm^{-1} . The B_{20} values calculated from the PL spectra at $\delta t = 720$ or $1200 \mu\text{s}$ are 910 and 1200 cm^{-1} , respectively.

According to Nishimura and Kushida,^{70,71} a major mechanism responsible for the 5D_0 – 7F_0 intensity in various europium-doped glasses is the mixing of the 7F_2 into the 7F_0 state through the $B_{20}C_0^{(2)}$ term of the crystal-field Hamiltonian. The ratio of the integrated intensities from the 5D_0 – 7F_0 and 5D_0 – 7F_2 transition can be approximated as⁷¹

$$\frac{I(^5D_0 - ^7F_0)}{I(^5D_0 - ^7F_2)} = \frac{4B_{20}^2}{375\Delta_{20}^2} \left[\frac{E(^5D_0 - ^7F_0)}{E(^5D_0 - ^7F_2)} \right]^3 \quad (6)$$

with $\Delta_{20} = 1036 \text{ cm}^{-1}$ being the energy separation between 7F_2 and 7F_0 of the free ion state and $E(^5D_0 - ^7F_0)$ and $E(^5D_0 - ^7F_2)$ the energies of the denoted transitions. For the $E(^5D_0 - ^7F_0)$ and $E(^5D_0 - ^7F_2)$ the peak emission at about $\lambda_{em} = 577.5$ and 615 nm measured from PL spectra measured at long delays ($\delta t \geq 1$ ms) were used, respectively, in the calculations. In contrast with estimation of $I(^5D_0 - ^7F_0)/I(^5D_0 - ^7F_2)$ ratio corresponding to the short-lived europium species, the estimation of this ratio corresponding to the long-lived europium species can be easily resolved from the PL spectra measured at long delays ($\delta t \geq 1$ ms) when the contribution of the short-lived species completely vanished. The experimental values for the $I(^5D_0 - ^7F_0)/I(^5D_0 - ^7F_2)$ ratio were estimated to about 0.026 – 0.030 . By using eqs 5 and 6, values between about 0.01 and 0.016 were obtained. Considering the effects of noise on the Gaussian deconvolution used for the calculation of B_{20} (eq 5), we can argue that the calculated ratio is of the same order of magnitude and close to the value estimated from the experimental data (0.026 – 0.030). Consequently, it can be concluded that the J -mixing of the 7F_2 into the 7F_0 state through the axial second-order crystal-field potential is the main mechanism responsible for the intensity observed for the 5D_0 – 7F_0 emission in europium–ZG materials.

III.2.1.3. 5D_0 – 7F_2 . In contrast to the 5D_0 – 7F_1 transition, the intensity of the forced electric dipole 5D_0 – 7F_2 transition is hypersensitive to the variation of the bonding environment of the europium ion. By using the intensity of the 5D_0 – 7F_1 transition as an internal reference, the intensity ratio $R = I(^5D_0 - ^7F_2)/I(^5D_0 - ^7F_1)$ increases with the degree of Eu^{3+} –O covalence or/and the increase of the local asymmetry.^{62,76} The R values of the europium in ZG determined from the prompt PL spectra (spectra measured at $\delta t = 2 \mu\text{s}$) are close to 1 for all the parent Zeogrid. A slight tendency of the R values to decrease with increasing Si/Al ratio was observed (Figure 2). This trend correlated well with the dependence of PL decays on the Si/Al ratio (Figure 7).

The R values estimated from the prompt PL spectra contain the contribution from both europium species which may exhibit

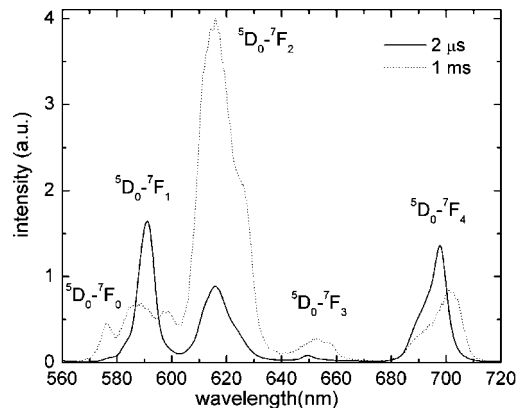


Figure 6. Time-resolved luminescence spectra of the parent Eu^{3+} –ZG(150) measured after delay times of $2 \mu\text{s}$ (solid line) and 1 ms (dotted line), respectively.

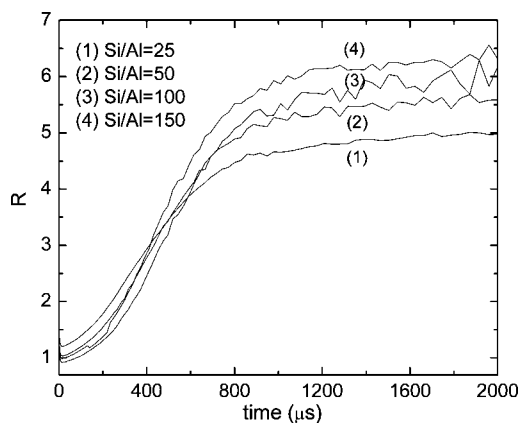


Figure 7. Time evolution of the intensity ratio R for the different Si to Al ratio in the parent Eu^{3+} –ZG.

quite different local environments and hence R values. This is well-illustrated with Figure 6 which presents the comparison between the prompt PL spectrum and that measured at $\delta t = 1$ ms. The different intensities ratios determined at two different time delays δt are clearly evidenced. Further, the splitting of the 7F_1 is strongly increased from a about 2 – 3 nm (about 90 cm^{-1}) measured from the prompt PL spectra to about 14 nm (about 400 cm^{-1}) measured from the delayed spectrum (see also Figure 5) which is associated with the long-lived europium species. This effect can be attributed to the increase of the crystal-field strength $N_\nu(B_{2q})$ at the long-lived europium sites according to the following equation defined by Malta:⁷⁷

$$\Delta E(^7F_1) = \sqrt{\frac{0.3}{\pi(2 + \alpha^2)}} N_\nu(B_{2q})$$

$$\alpha = \frac{E_b - E_c}{\Delta E/2} \quad (7)$$

where E_b refers to the barycenter, E_c is the energy position of the central 7F_1 Stark level, and ΔE is the maximum Stark splitting of the 7F_1 level. Further, the crystal-field strength $N_\nu(B_{2q})$ can be defined in terms of the second-rank crystal-field parameters as⁷⁸

$$N_\nu(B_{2q}) = \sqrt{\frac{4\pi}{5}(B_{20}^2 + 2B_{22}^2)} \quad (8)$$

The estimation of the R value associated with long-lived species (R_L) is straightforward and is determined as $5.0 < R_L < 6.2$ when increasing the Si/Al ratio from 25 to 150 . A better

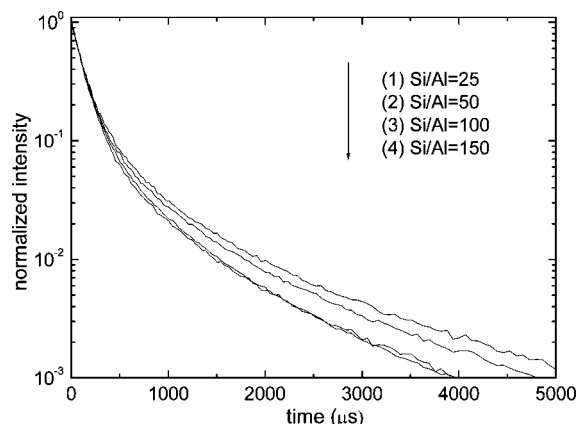


Figure 8. Effects of the Si to Al ratio on the PL decays of the parent Eu^{3+} -ZG.

visualization of the time evolution of R values is represented in Figure 7. The curves show the saturation of the R_L values after about $\delta t = 1$ ms, when the luminescence of the short-lived europium species is quenched, at $R_L = 5, 5.4, 5.8$, and 6.2 for the Si/Al ratio = 25, 50, 100, and 150. The saturation values of R_L appear to be on the upper side of the R range commonly found for europium-doped glasses ($R = 3$ – 6)^{64,79–81} and indicate that the long-lived europium species are located in highly distorted sites in the parent ZG.

To estimate the R value related to the short-lived europium species (R_S) we needed to estimate the relative contributions of the two europium species to the total emission. Such an estimation was inferred from the analysis of the PL decays. The PL decays of the parent europium-ZG measured at $\lambda_{\text{em}} = 614$ nm following non-selective excitation at $\lambda_{\text{ex}} = 394$ nm were non-exponential. In the present paper, the PL decays are discussed only in relation with the europium species distribution and silylation effects. A detailed analysis of the PL decays in line with our recently published work⁴² will be presented elsewhere. Both fitting methods, the discrete exponential analysis and the quantified entropy method (see the Experimental Section), pointed to two major lifetime components or a bimodal distribution of lifetimes while a third life-long component (1.5–1.7 ms) with a very small amplitude (about 5% of the total amplitude) seemed to be present in all PL decays. The values of the two lifetimes are centered around $110 \mu\text{s} < \tau_S < 125 \mu\text{s}$ and $420 \mu\text{s} < \tau_L < 460 \mu\text{s}$ and represent the lifetimes of the short- and long-lived europium species, respectively. The short-lived europium species has the dominant contribution to the total PL with its amplitude increasing from about 0.75 (Si to Al = 25) to 0.9 (Si to Al = 150). As a result, the overall PL decays became faster with the increasing Si/Al ratio (Figure 8), a trend already observed with terbium in another microporous-mesoporous MFI-type material, Zeotile-1.³⁸ This is reflected in the increasing of the average lifetime by almost 20% across the Si/Al range (Table 2).

The time dependence of the intensities ratio, R , can be approximated by the following equation:

$$R(t) = \frac{A_{0-2}(t)}{A_{0-1}(t)} = \frac{A_{0-2S} \exp(-t/\tau_S) + A_{0-2L} \exp(-t/\tau_L)}{A_{0-1S} \exp(-t/\tau_S) + A_{0-1L} \exp(-t/\tau_L)} \quad (9)$$

where S and L denote the short- and long-lived europium species, A_{0-2S} , A_{0-1S} , A_{0-2L} , and A_{0-1L} refer to the contribution of the short- or long-lived europium species to the integrated intensities of $^5\text{D}_0$ - $^7\text{F}_2$ and $^5\text{D}_0$ - $^7\text{F}_1$ transitions, respectively, and τ_S or τ_L are the lifetimes of the short- and long-lived europium species, respectively. The fractional amplitudes derived from the fitting of the PL decays were further related to the relative contribution of the short- and long-lived europium species to the $^5\text{D}_0$ - $^7\text{F}_1$ emission. The R_L values (defined as $R_L = A_{0-2L}/A_{0-1L}$) were determined from the experimental PL spectra at $\delta t = 1.2$ ms (see also Figure 7). By using eq 6, the R_S values (defined as $R_S = A_{0-2S}/A_{0-1S}$) were found to increase from about $R_S = 0.36$ – 0.45 (Si/Al = 150) up to $R_S = 0.62$ – 0.68 (Si/Al = 25). The R_S values are close to those reported for EuCl_3 in silica ($R = 0.43$)⁶⁴ or to those measured for the free europium in water ($R = 0.6$). Further, the lifetime associated with this species ($110 \mu\text{s} < \tau_S < 125 \mu\text{s}$) is close to that measured for a free europium ion in water ($\tau = 105 \pm 10 \mu\text{s}$). We conclude that the nature of the short-lived europium species in parent ZG is close to a fully hydrated europium ion.

In the case of the multiple emissive species it is further expected that the PL decay varies across the emission band. A strong variation of the PL decay was observed across the $^5\text{D}_0$ - $^7\text{F}_1$ emission band. Figure 9 illustrates the PL decays measured at three different emission wavelengths within this emission. The PL decays were found to be shortest at $\lambda_{\text{em}} = 586$ nm and increased at $\lambda_{\text{em}} = 590$ or 598 nm. The PL decay measured at $\lambda_{\text{em}} = 590$ nm was related to the short-lived species while those measured at the edges of $^5\text{D}_0$ - $^7\text{F}_1$ emission ($\lambda_{\text{em}} = 586$ and 598 nm) could be attributed to the long-lived species. These assignments agree with those obtained from the TRES analysis (Figure 5).

Following non-selective excitation at $\lambda_{\text{ex}} = 394$ nm, besides the emission from the $^5\text{D}_0$ state, emission related to the $^5\text{D}_1$ state was also observed (Figure 2). Emission from the $^5\text{D}_1$ is caused by the low phonon energy of the host which decelerates the nonradiative relaxation from $^5\text{D}_1$ to the main emitting level $^5\text{D}_0$. It is generally established that the $^5\text{D}_1$ - $^7\text{F}_1$ transition is almost an electric dipole, whereas in the $^5\text{D}_1$ - $^7\text{F}_0$ transition the magnetic dipole nature dominates.⁷² The average lifetime of this level is only a few microseconds, as no PL from this level is detected after $\delta t = 20 \mu\text{s}$ (in both parent and silylated ZG). Similar to the $^5\text{D}_0$ level, the relative intensities of the $^5\text{D}_1$ - $^7\text{F}_{0,1,2}$ transitions show a dependency on the Si/Al ratio but to a smaller extent (Figure 10).

III.2.2. Silylated Europium-ZG. Following silylation, the following modifications of both PL spectra (Figure 11) and decays (Figure 12) were observed (see also Table 2): (i) the intensity ratio corresponding to $^5\text{D}_0$ - $^7\text{F}_0$ and $^5\text{D}_0$ - $^7\text{F}_1$ transitions is increased by a factor of up to 6 (at Si/Al = 150); (ii) the R value is increased from about 1 in the parent Eu-ZG to 1.9 (at

TABLE 2: Comparison between the Intensity Ratios Associated with the $^5\text{D}_0$ - $^7\text{F}_0$, $^5\text{D}_0$ - $^7\text{F}_1$, $^5\text{D}_0$ - $^7\text{F}_2$, $^5\text{D}_1$ - $^7\text{F}_1$, and $^5\text{D}_1$ - $^7\text{F}_0$ Transitions and Average Lifetimes Measured with Parent (P) and Silylated (S) Europium-ZG

Si/Al	$I(^5\text{D}_0-^7\text{F}_2)/I(^5\text{D}_0-^7\text{F}_1)$		$I(^5\text{D}_1-^7\text{F}_1)/I(^5\text{D}_1-^7\text{F}_0)$		$I(^5\text{D}_0-^7\text{F}_0)/I(^5\text{D}_0-^7\text{F}_1)$		average PL lifetime $\langle \tau \rangle$ (μs)	
	P	S	P	S	P	S	P	S
25	1.3	2.3	2	3.2	0.03	0.05	203	320
50	1.1	1.9	3.5	6.8	0.03	0.06	190	280
100	0.95	2.4	3.5	7.5	0.02	0.12	162	240
150	0.95	3.5	3.5	10	0.02	0.12	166	245

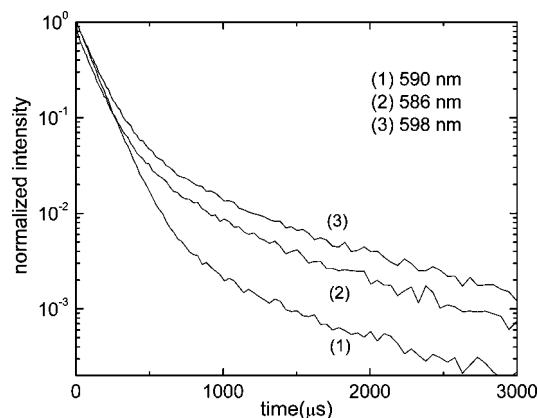


Figure 9. Dependency of the PL decays of parent Eu³⁺-ZG(150) on the emission wavelength across the ⁵D₀-⁷F₁ transition.

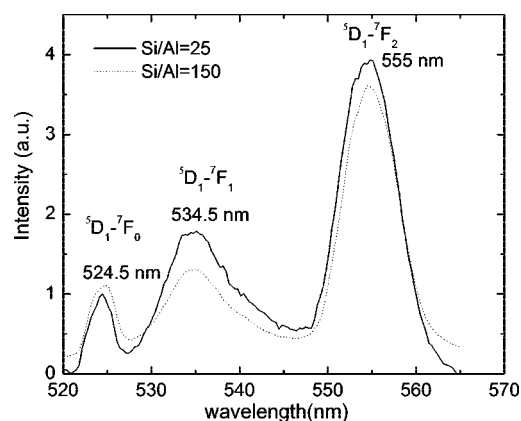


Figure 10. Comparison between PL spectra of the parent Eu³⁺-ZG(25) and Eu³⁺-ZG(150) in the range of the ⁵D₁ emission.

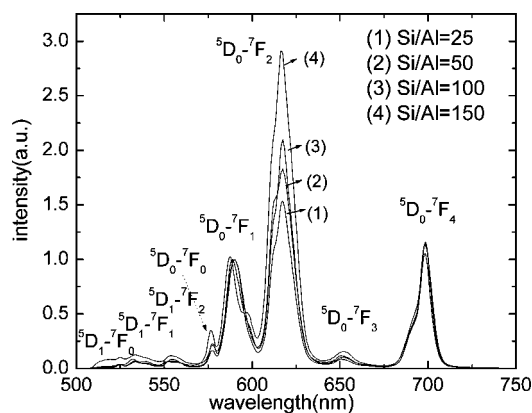


Figure 11. Effects of the Si to Al ratio on the PL spectra of the silylated Eu³⁺-ZG. All spectra were normalized to the area corresponding to the ⁵D₀-⁷F₁ transition.

Si/Al = 50) and 3.5 (at Si/Al = 150). The maximum R value of 3.5 is at the lower side of the range usually found in oxide glasses.⁸⁰ These values indicate that the average environment of the europium ions in the silylated ZG is of low symmetry; (iii) the PL spectra get a more structured line shape which is best exemplified for the ⁵D₀-⁷F₁ emission; (iv) the PL decays are lengthened and show greater dispersion with the Si/Al ratio.

Following non-selective excitation at $\lambda_{\text{ex}} = 394$ nm, all measured PL decays of the silylated europium-ZG were non-exponential. The PL decays were satisfactorily fitted with two exponentials or a bimodal-type distribution with lifetimes of $160 \mu\text{s} < \tau_s < 180 \mu\text{s}$ and $480 \mu\text{s} < \tau_L < 560 \mu\text{s}$. The contribution of the short-lived europium species remained

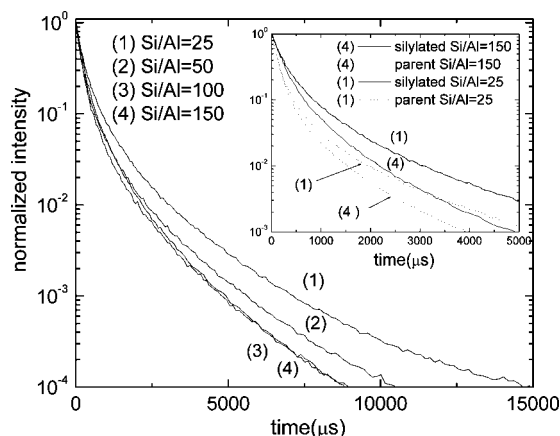


Figure 12. Effects of the Si to Al ratio on the PL decays of silylated Eu³⁺-ZG. Inset: effects of silylation on the PL decays of Eu³⁺-ZG(25) and Eu³⁺-ZG(150).

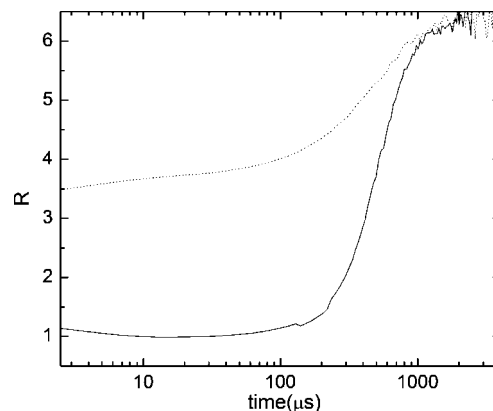


Figure 13. Effects of the silylation on the time evolution of intensity ratio R for Eu-ZG(150) (solid line, parent; dotted line, silylated).

dominant decreasing from about 75% (Si/Al = 150) to 65% (Si/Al = 25). The average lifetime is increased by 50% (at Si/Al = 150) and up to 60% (at Si/Al = 25) (Table 2 and Figure 12) compared to the parent materials.

For the estimation of the R value related to the short-lived europium species (R_s) we have applied the same procedure used for the parent Zeogrid. We found that the R_s values increase from 1.0–1.1 (Si/Al = 25) up to 2.0–2.4 for Si/Al = 150. These values indicate that, compared to the parent Zeogrid, the short-lived europium species in the silylated ZG is also located in relatively distorted sites. For the long-lived europium species we found that after $\delta t = 1$ –1.2 ms the R_L values saturate at the same values (R_L) for the parent and silylated Zeogrid, namely, at 5 (Si/Al = 25) or 6.2 (Si/Al = 150) (Figure 13).

The similar R_L values measured from the PL spectra of both parent and silylated ZG advocate for the similar local environments of the long-lived europium species in the two materials. Further evidence is given by the comparison of the PL spectra of europium in the parent and silylated Zeogrid measured at $\delta t = 1.2$ ms. From the insets of Figures 14 and 15 it is clear that the two spectra are similar, with similar splitting structure in the region of the ⁵D₀-⁷F₁ emission. A similar Stark level structure for the ⁵D₀-⁷F₁ transition leads to similar second-rank crystal-field parameter values (eq 4) as well as crystal-field strength in both parent and silylated Zeogrid. The increased lifetimes and amplitudes obtained for silylated europium-ZG ($480 \mu\text{s} < \tau_L < 560 \mu\text{s}$) compared to the parent ZG ($420 \mu\text{s} < \tau_L < 460 \mu\text{s}$) can be explained by an increased contribution of the framework oxygens over those from OH groups in the first

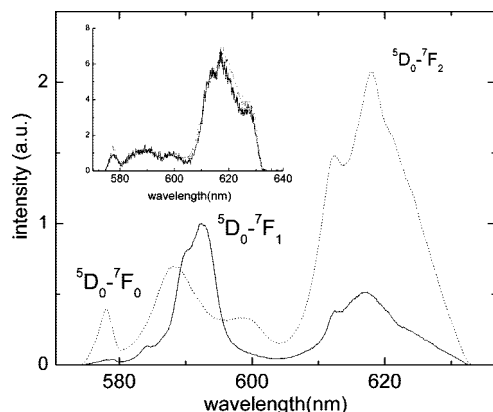


Figure 14. Comparison between the PL spectra of the parent (solid line) and silylated (dotted line) Eu^{3+} -ZG(150) measured at 2 μs after the laser pulse. Inset: comparison between the PL spectra of the parent (solid line) and silylated (dotted line) Eu^{3+} -ZG(150) measured at 1.2 ms after the laser pulse.

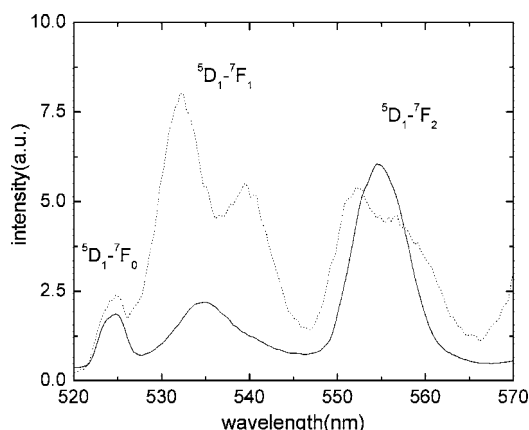


Figure 15. Effects of the silylation on the $^5\text{D}_1$ emission for Eu^{3+} -ZG(150) (solid line, parent; dotted line, silylated).

coordination shell of the long-lived europium species. The pore size of the parent ZG is about 1.4–1.5 nm which is decreased in average by almost 45% upon silylation using the C_{16} agent. This makes the silylating agent C_{16} efficient in protecting europium ions located inside the pores against rehydration effects. On the other hand, the short-lived species are of different nature in the parent and silylated Zeogrid. In the parent Zeogrid a close to a fully hydrated europium species is found based on the R_S values of 0.34–0.68 and the PL lifetimes of $110 \mu\text{s} < \tau_S < 125 \mu\text{s}$. This is further supported by the apparent low nephelauxetic effect. For a fully hydrated europium complex the $^5\text{D}_0$ – $^7\text{F}_0$ transition energy was determined at $17\,280 \text{ cm}^{-1}$.⁸¹ In the present study $^5\text{D}_0$ – $^7\text{F}_0$ transition energies around $17\,274 \text{ cm}^{-1}$ ($\lambda = 578.9 \text{ nm}$) were found which indicate a small nephelauxetic effect of the ligands present, which is typical for highly hydrated Eu^{3+} complexes. In the silylated Zeogrid, R_S values increased up to 1.0–2.4 suggesting relatively distorted environments. Further, the lifetimes increased to $160 \mu\text{s} < \tau_S < 180 \mu\text{s}$ which sustains a mixed bonding of europium to water molecules and oxygen atoms of the Zeogrid framework. This clearly indicates that silylation protects europium ions against water intrusion on the internal surface as well as inside the pores. The average PL lifetimes of europium in the silylated ZG come close to those obtained for a ternary europium complex covalently linked to the mesoporous SBA-15 ($0.32 \text{ ms} < \tau < 0.49 \text{ ms}$)²² or to europium–diketonate impregnated on the cubic MCM-48 ($\tau = 370 \mu\text{s}$).²⁰

The shortening of the europium PL decays with increasing the Si to Al ratio can be attributed to the increased contribution of the europium ions located on the internal surface in both parent and silylated Zeogrid (see also Table 1). The increased average PL lifetimes in the silylated ZG compared to those measured with parent ZG are attributed to the reduced contribution of the –OH groups in the first coordination shell of europium. Such effect is assigned to the capability of the hexadecyl group to block the water intrusion at the europium sites.

The ratio of the integrated intensities corresponding to $^5\text{D}_1$ – $^7\text{F}_1$ and $^5\text{D}_1$ – $^7\text{F}_0$ is increasing by a factor of about 3, from 3.5 in the parent europium–ZG(150) up to 10 in the silylated. Strong hypersensitivity effects can thus be observed with the $^5\text{D}_1$ emission. However, any considerations regarding Stark structure, even for the $^5\text{D}_1$ – $^7\text{F}_0$ transition, were hindered by the low quantum efficiency of this $^5\text{D}_1$ emission.

Besides asymmetry effects, the covalency of the oxygen-type ligand field can also contribute to the changes of the R values across the europium species. In the parent or silylated Zeogrid, the europium comprises two different types of oxygen-based environments with an increased contribution of the oxygen atoms from ZG framework relative to those from the water molecules for the long-lived europium species compared to the short-lived europium species. This observation corroborated with the assertion that the bonding between europium and oxygen atoms of the ZG framework has a more covalent nature compared to the oxygen ions from water molecules^{81,82} may sustain a more covalent bonding environment for the long-lived europium species. No correlation between the increase of the R values corresponding to the long-lived europium species R_L (about 5–6.2) relative to those corresponding the short-lived europium species R_S (0.36–2.4) and the nephelauxetic effect could be found in either parent and silylated Eu –ZG. As seen from the Figure 4, parts a and b, the $^5\text{D}_0$ – $^7\text{F}_0$ emission corresponding to the long-lived europium species is blue-shifted (at about 577.5 nm) relative to that corresponding to the short-lived europium species (at 578.7 nm in the parent Zeogrid). We can only speculate that the covalency effects exhibited by the europium ions in Zeogrid are small as clear interpretation regarding the correlation between the nephelauxetic and covalency effects needs still to be found.^{83,84}

IV. Conclusions

The PL properties of europium in the parent (non-silylated) and silylated Zeogrid were investigated in detail in relation to the Zeogrid structure. The results can be summarized as follows: (i) Two major europium species were found with each europium species comprehensively characterized in terms of local crystal field and symmetry as well as the constitution of the first hydration shell. Thus, in the parent Zeogrid a close to fully hydrated europium species was determined characterized by asymmetry value R_S of 0.34–0.68, lifetimes of $110 \mu\text{s} < \tau_S < 125 \mu\text{s}$, and $^5\text{D}_0$ – $^7\text{F}_0$ transition energies around $17\,274 \text{ cm}^{-1}$. In the silylated Zeogrid, R_S values increase up to 1.0–2.4 suggesting a relatively distorted environment. Further, the lifetimes increased to $160 \mu\text{s} < \tau_S < 180 \mu\text{s}$ which sustains a mixed bonding of europium with water and oxygen atoms of the Zeogrid framework in the silylated materials. The long-lived europium species experience similar crystal-field strength in the parent and silylated Zeogrid. The asymmetry values associated to this species are found to be analogous in the parent and silylated Zeogrid and increased from $R_L = 5$ –6.2 with increasing Si/Al ratio from 25 to 150. The increased lifetimes and

amplitudes obtained following silylation ($\tau_L = 480 \mu\text{s} < \tau_L < 560 \mu\text{s}$) compared to those measured with the parent Zeogrid ($420 \mu\text{s} < \tau_L < 460 \mu\text{s}$) are explained by an increased contribution of the framework oxygen atoms over the water ligands in the first coordination shell of the long-lived europium species. (ii) The mechanism determining the intensity of the electric and magnetic forbidden $^5D_0 \rightarrow ^7F_0$ transition was attributed to the J -mixing of the 7F_2 into the 7F_0 state through the axial second-order crystal-field potential. (iii) The comparison between the europium average PL lifetimes and the relative intensities of emission transitions related to 5D_0 level corresponding to the parent and silylated europium–Zeogrid gives strong support for the efficiency of silylation in diminishing the adverse effects of rehydration on the europium PL properties. Thus, following silylation the average PL lifetimes increased by 50% for (Si/Al = 150) up to 60% (Si/Al = 25).

References and Notes

- (1) Kresge, T.; Leonowicz, M. E.; Roth, W. J.; Vartuli, J. C.; Beck, J. S. *Nature* **1992**, 359, 710.
- (2) Beck, J. S.; Vartuli, J. C.; Roth, W. J.; Leonowicz, M. E.; Kresge, K. T.; Schmitt, K. D.; Chu, C. T. W.; Olson, D. H.; Sheppard, E. W.; McCullen, S. B.; Higgins, J. B.; Schlenker, J. L. *J. Am. Chem. Soc.* **1992**, 114, 10834.
- (3) Corma, A. *Chem. Rev.* **1997**, 97, 2373.
- (4) Vogt, E. T. C.; Kresge, C. T.; Vartuli, J. C. In *Introduction to Zeolite Science and Practice*; van Bekkum, H.; Flanigen, E. M.; Jacobs, P. A., Jansen, J. C., Eds.; Elsevier Science Ltd.: Amsterdam, 2001; p 1003.
- (5) Di Renzo, F.; Galarneau, A.; Trens, P.; Fajula, F. In *Handbook of Porous Solids*; Schuth, F., Sing, K. S. W., Weitkamp, J., Eds.; Wiley-VCH: Weinheim, Germany, 2002; Vol. 3, p 1311.
- (6) Kaskel, S. In *Handbook of Porous Solids*; Schuth, F., Sing, K. S. W., Weitkamp, J., Eds.; Wiley-VCH: Weinheim, Germany, 2002; Vol. 3, p 1190.
- (7) Taguchi, A.; Schuth, F. *Microporous Mesoporous Mater.* **2005**, 77, 1.
- (8) Ariga, K.; Vinu, A.; Hill, J. P.; Mori, T. *Coord. Chem. Rev.* **2007**, 251, 2562.
- (9) Corriu, R. J. P.; Mehdi, A.; Reyé, C.; Thieuleux, C.; Frenkel, A.; Gibaud, A. *New J. Chem.* **2004**, 28, 156.
- (10) Fernandes, A.; Dexpert-Ghys, J.; Gleizes, A.; Galarneau, A.; Brunel, D. *Microporous Mesoporous Mater.* **2005**, 83, 35.
- (11) Fu, L.; Xu, Q.; Zhang, H.; Li, L.; Meng, Q.; Xu, R. *Mater. Sci. Eng., B* **2002**, 88, 68.
- (12) Yan, B.; Zhou, B. *J. Photochem. Photobiol., A* **2008**, 195, 314.
- (13) Gago, S.; Fernandes, J. A.; Rainho, J. P.; Sá Ferreira, R. A.; Pillinger, M.; Valente, A.; Santos, M.; Carlos, L. D.; Ribeiro-Claro, P. J. A.; Gonçalves, I. S. *Chem. Mater.* **2005**, 17, 5077.
- (14) Gleizes, A. N.; Fernandes, A.; Dexpert-Ghys, J. *J. Alloys Compd.* **2004**, 374, 303.
- (15) Guo, X.; Fu, L.; Zhang, H.; Carlos, L. D.; Peng, C.; Guo, J.; Yu, J.; Deng, R.; Sun, L. *New J. Chem.* **2005**, 29, 1351.
- (16) Li, H. R.; Lin, J.; Fu, L. S.; Guo, J. F.; Meng, Q. G.; Liu, F. Y.; Zhang, H. *J. Microporous Mesoporous Mater.* **2002**, 55, 103.
- (17) Binnemans, K.; Lenaerts, P.; Driesen, K.; Gorrler-Walrand, C. *J. Mater. Chem.* **2004**, 14, 191.
- (18) Matos, J. R.; Mercuri, L. P.; Jaroniec, M.; Kruk, M.; Sakamoto, Y.; Terasaki, O. *J. Mater. Chem.* **2001**, 11, 2580.
- (19) Meng, Q.; Boutinaud, P.; Zhang, H.; Mahiou, R. *J. Lumin.* **2007**, 124, 15.
- (20) Meng, Q. G.; Boutinaud, P.; Franville, A.; Zhang, H. J.; Mahiou, R. *Microporous Mesoporous Mater.* **2003**, 65, 127.
- (21) Peng, C.; Zhang, H.; Meng, Q.; Li, H.; Yu, J.; Guo, J.; Sun, L. *Inorg. Chem. Commun.* **2005**, 8, 440.
- (22) Peng, C.; Zhang, H.; Yu, J.; Meng, Q.; Fu, L.; Li, H.; Sun, L.; Guo, X. *J. Phys. Chem. B* **2005**, 109, 15278.
- (23) Xu, Q.; Li, L.; Li, B.; Yu, J.; Xu, R. *Microporous Mesoporous Mater.* **2000**, 38, 351.
- (24) Xu, Q.; Li, L.; Liu, X.; Xu, R. *Chem. Mater.* **2002**, 14, 549.
- (25) Xu, W.; Luo, Q.; Wang, H.; Francesconi, L. C.; Stark, R. E.; Akins, D. L. *J. Phys. Chem. B* **2003**, 107, 497.
- (26) Zhang, M.; Yin, W.; Su, Q.; Zhang, H. *Mater. Lett.* **2002**, 57, 940.
- (27) Zhang, X.; Zhang, C.; Guo, H.; Huang, W.; Polenova, T.; Francesconi, L. C.; Akins, D. L. *J. Phys. Chem. B* **2005**, 109, 19156.
- (28) Zhou, Y.; Bao, R.; Yue, B.; Gu, M.; Pei, S.; He, H. *J. Mol. Catal. A: Chem.* **2007**, 270, 50.
- (29) Sun, L.; Yu, J.; Zhang, H.; Meng, Q.; Ma, E.; Peng, C.; Yang, K. *Microporous Mesoporous Mater.* **2007**, 98, 156.
- (30) Stein, A.; Melde, B. J.; Schroden, R. C. *Adv. Mater.* **2000**, 12 (19), 1403.
- (31) Takei, T.; Houshito, O.; Yonesaki, Y.; Kumada, N.; Kinomura, N. *J. Solid State Chem.* **2007**, 180, 1180.
- (32) Nishiyama, N.; Park, D. H.; Egashira, Y.; Ueyama, K. *Sep. Purif. Technol.* **2003**, 32, 127.
- (33) Yang, H.; Zhang, L.; Su, W.; Yang, Q.; Li, C. *J. Catal.* **2007**, 248, 204.
- (34) Yang, H.; Zhang, G.; Hong, X.; Zhu, Y. *Microporous Mesoporous Mater.* **2004**, 568, 119.
- (35) Aoyama, N.; Yoshihara, T.; Furukawa, S.; Nitta, T.; Takahashi, H.; Nakano, M. *Fluid Phase Equilib.* **2007**, 257, 212.
- (36) Scott, B. J.; Wirsberger, G.; Stucky, G. D. *Chem. Mater.* **2001**, 13, 3140.
- (37) Maas, H.; Currao, A.; Calzaferri, G. *Angew. Chem., Int. Ed.* **2002**, 41, 2495.
- (38) Tiseanu, C.; Kumke, M. U.; Parvulescu, V. I.; Gessner, A.; Gagea, B. C.; Martens, J. A. *J. Phys. Chem. B* **2006**, 110, 25707.
- (39) Tiseanu, C.; Gessner, A.; Kumke, M. U. *J. Non-Cryst. Solids* **2008**, 354, 1969.
- (40) Tiseanu, C.; Gessner, A.; Kumke, M. U.; Gagea, B.; Parvulescu, V. I. *J. Lumin.* **2008**, 128, 751.
- (41) Tiseanu, C.; Gessner, A.; Kumke, M. U.; Gagea, B.; Parvulescu, V. I. *J. Appl. Phys.* Accepted for publication 2008.
- (42) Tiseanu, C.; Gagea, B.; Parvulescu, V. I.; Lórenz-Fonfría, V.; Gessner, A.; Kumke, M. U. *Langmuir* **2007**, 23, 6781.
- (43) Tiseanu, C.; Gessner, A.; Kumke, M.; Lórenz-Fonfría, V. A.; Gagea, B. *J. Mater. Sci.: Mater. Electron.* [Online early access]. DOI: 10.1007/s10854-008-9597-1.
- (44) Kremer, S. P. B.; Kirschhock, C. E. A.; Jacobs, P. A.; Martens, J. A. C. *R. Chim.* **2005**, 8, 379.
- (45) Aerts, A.; van Isacker, A.; Huybrechts, W.; Kremer, S. P. B.; Kirschhock, C. E. A.; Collignon, F.; Houthoofd, K.; Denayer, J. F. M.; Baron, G. V.; Marin, G. B.; Jacobs, P. A.; Martens, J. A. *Appl. Catal., A* **2004**, 257, 7.
- (46) Kremer, S. P. B.; Kirschhock, C. E. A.; Tielen, M.; Collignon, F.; Grobet, P. J.; Jacobs, P. A.; Martens, J. A. *Adv. Funct. Mater.* **2002**, 12, 286.
- (47) Kirschhock, C. E. A.; Buschmann, V.; Kremer, S.; Ravishanker, R.; Houssin, C. J. Y.; Mojet, B. L.; van Santen, R. A.; Grobet, P. J.; Jacobs, P. A.; Martens, J. A. *Angew. Chem., Int. Ed.* **2001**, 40, 2637.
- (48) Durville, F.; Boulon, G.; Reisfeld, R.; Mack, H.; Jorgensen, C. K. *Chem. Phys. Lett.* **1983**, 102, 393.
- (49) (a) Babu, P.; Jayasankar, C. K. *Physica B* **2000**, 279, 262. (b) Bettinelli, M.; Speghini, A.; Ferrari, M.; Montagna, M. *J. Non-Cryst. Solids* **1996**, 201, 211.
- (50) Biswas, A.; Friend, C. S.; MacIel, G. S.; Prasad, P. N. *J. Non-Cryst. Solids* **2000**, 261, 9.
- (51) Campostrini, R.; Carturan, G.; Ferrari, M.; Montagna, M.; Pilla, O. *J. Mater. Res.* **1992**, 7, 745.
- (52) Cormier, G.; Capobianco, J. A.; Monteil, A. *J. Non-Cryst. Solids* **1993**, 152, 225.
- (53) Ebendorff-Heidepriem, H.; Ehr, D. *J. Non-Cryst. Solids* **1996**, 208, 205.
- (54) Fujita, K.; Tanaka, K.; Hirao, K.; Soga, N. *Opt. Lett.* **1998**, 23, 543.
- (55) Hreniak, D.; Zych, E.; Kępiński, L.; Strek, W. *J. Phys. Chem. Solids* **2003**, 64, 111.
- (56) Inoue, H.; Soga, K.; Makishima, A. *J. Non-Cryst. Solids* **1997**, 222, 212.
- (57) Lochhead, M. J.; Bray, K. L. *Chem. Mater.* **1995**, 7, 572.
- (58) Ray, S.; Pramanik, P.; Singha, A.; Roy, A. *J. Appl. Phys.* **2005**, 97, 094312/1.
- (59) Nageno, Y.; Takebe, H.; Morinaga, K.; Izumitani, T. *J. Non-Cryst. Solids* **1994**, 169, 288.
- (60) Nogami, M.; Nagakura, T.; Hayakawa, T. *J. Lumin.* **2000**, 86, 117.
- (61) Nogami, M.; Yamazaki, T.; Abe, Y. *J. Lumin.* **1998**, 7, 8–63.
- (62) Oomen, E. W. J. L.; van Dongen, A. M. A. *J. Non-Cryst. Solids* **1989**, 111, 205.
- (63) Reisfeld, R.; Saraidarov, T.; Pietraszkiewicz, M.; Lis, S. *Chem. Phys. Lett.* **2001**, 349, 266.
- (64) Reisfeld, R.; Zigansky, E.; Gaft, M. *Mol. Phys.* **2004**, 102, 1319.
- (65) Schmechel, R.; Kennedy, M.; VonSeggern, H.; Winkler, H.; Kolbe, M.; Fischer, R. A.; Xiaomao, L.; Benker, A.; Winterer, M.; Hahn, H. *J. Appl. Phys.* **2001**, 89, 1679.
- (66) Tanaka, M.; Nishimura, G.; Kushida, T. *Phys. Rev. B* **1994**, 49, 16917.
- (67) Brochon, J. C. In *Methods in Enzymology*; Johnson, M. L., Brands, L., Eds.; Academic Press: San Diego, CA, 1994; Vol. 240.
- (68) Capobianco, J. A.; Proulx, P. P.; Bettinelli, M.; Negrosolo, F. *Phys. Rev. B* **1990**, 42, 5936.
- (69) Rolli, R.; Samoggia, G.; Bettinelli, M.; Speghini, A.; Wachtler, M. *J. Non-Cryst. Solids* **2001**, 288, 114.

- (70) Nishimura, G.; Kushida, T. *Phys. Rev. B* **1988**, 37, 9075.
(71) Nishimura, G.; Kushida, T. *J. Phys. Soc. Jpn.* **1991**, 60, 683.
(72) Kushida, T.; Tanaka, M. *Phys. Rev. B* **2002**, 65, 195118/1.
(73) Brecher, C.; Riseberg, L. A. *Phys. Rev. B* **1976**, 13, 81.
(74) Lempicki, A.; Samelson, H.; Brecher, C. *J. Mol. Spectrosc.* **1968**, 27, 375.
(75) Pucker, G.; Gatterer, K.; Fritzer, H. P.; Bettinelli, M.; Ferrari, M. *Phys. Rev. B* **1996**, 53, 6225.
(76) Reisfeld, R.; Greenberg, E.; Brown, R. N.; Drexhage, M. G.; Jørgensen, C. K. *Chem. Phys. Lett.* **1983**, 95, 91.
(77) Malta, O. L.; Antic-Fidancev, E.; Lemaitre-Blaise, M.; Milicic-Tang, A.; Taibi, M. *J. Alloys Compd.* **1995**, 228, 41.
(78) Auzel, F. *Mater. Res. Bull.* **1979**, 14, 223.
(79) Rice, D. K.; DeShazer, L. G. *Phys. Rev.* **1969**, 186, 387.
(80) Gatterer, K.; Pucker, G.; Fritzer, H. P. *Phys. Chem. Glasses* **1997**, 38, 293.
(81) Frey, S. T.; Horrocks, W.; De, W., Jr. *Inorg. Chim. Acta* **1995**, 229, 383.
(82) Malta, O. L.; Batista, H. J.; Carlos, L. D. *Chem. Phys.* **2002**, 282, 21.
(83) Gorller-Walrand, C.; Binnemans, K. Spectral Intensities of f-f In *Handbook on the Chemistry and Physics of Rare Earths*; Gschneidner, K. A., Jr., Eyring, L., Eds.; North-Holland: Amsterdam, 1998; Vol. 25, Chapter 167.
(84) Choppin, G. R. *J. Alloys Compd.* **2002**, 344, 55.

JP711337H